



Published in final edited form as:

Neuroimage. 2015 January 15; 105: 369–379. doi:10.1016/j.neuroimage.2014.10.030.

Quantitative separation of arterial and venous cerebral blood volume increases during voluntary locomotion

Bing-Xing Huo¹, Yu-Rong Gao^{1,2}, and Patrick J. Drew^{1,2,3}

¹Center for Neural Engineering, Department of Engineering Science and Mechanics, Pennsylvania State University, University Park, PA 16802

²Neuroscience Graduate Program, Huck Institutes of the Life Sciences, Pennsylvania State University, University Park, PA 16802

³Department of Neurosurgery, Pennsylvania State University, University Park, PA 16802

Abstract

Voluntary locomotion is accompanied by large increases in cortical activity and localized increases in cerebral blood volume (CBV). We sought to quantitatively determine the spatial and temporal dynamics of voluntary locomotion-evoked cerebral hemodynamic changes. We measured single vessel dilations using two-photon microscopy and cortex-wide changes in CBV-related signal using intrinsic optical signal (IOS) imaging in head-fixed mice freely locomoting on a spherical treadmill. During bouts of locomotion, arteries dilated rapidly, while veins distended slightly and recovered slowly. The dynamics of diameter changes of both vessel types could be captured using a simple linear convolution model. Using these single vessel measurements, we developed a novel analysis approach to separate out spatially and temporally distinct arterial and venous components of the location-specific hemodynamic response functions (HRF) for IOS. The HRF of each pixel of was well fit by a sum of a fast arterial and a slow venous component. The HRFs of pixels in the limb representations of somatosensory cortex had a large arterial contribution, while in the frontal cortex the arterial contribution to the HRF was negligible. The venous contribution was much less localized, and was substantial in the frontal cortex. The spatial pattern and amplitude of these HRFs in response to locomotion in the cortex was robust across imaging sessions. Separating the more localized, arterial component from the diffuse venous signals will be useful for dealing with the dynamic signals generated by naturalistic stimuli.

Keywords

hemodynamics; linear model; two-photon microscopy; intrinsic optical imaging; exercise

Corresponding author: Patrick J. Drew, pjd17@psu.edu., Address: Center for Neural Engineering, Department of Engineering Science and Mechanics, Pennsylvania State University, University Park, PA 16802.

Conflict of Interest: None

Introduction

Changes in cerebral blood volume, flow, and oxygenation are widely used to infer neural activity (Logothetis, 2008). Because increases in neural activity, which can last for only a few milliseconds, are usually much briefer than the hemodynamic response, which evolves over seconds, it is necessary to use a quantitative model to relate the two. The hemodynamic signal is usually assumed to be a convolution of neural activity or sensory stimulus with the hemodynamic response function (HRF, also known as a kernel) (Boynton et al., 1996; Friston et al., 1994; Glover, 1999; Vazquez and Noll, 1998; Hirano et al., 2011; Logothetis et al., 2001; Martindale et al., 2003). Typically, the HRF is fit with a gamma distribution function (Boynton et al., 1996; Hirano et al., 2011), but there is evidence that the CBV HRF may be the sum of multiple components (Silva et al., 2007). Because HRFs differ across cortical location (Handwerker et al., 2004), and layer (Hirano et al., 2011), potentially due to neural and vascular differences (Tsai et al., 2009), it is useful to mechanistically understand their vascular origin.

The CBV HRF will be determined by the dynamics of volume changes in various vascular compartments. Arterial dilation, which is mediated by smooth muscle relaxation and is thought to be under the control of neural activity, follows stimulation within a second (Hillman et al., 2007; Kim et al., 2007; Drew et al., 2011; Tian et al., 2010). The distention of veins takes place over tens of seconds in response to prolonged stimuli (Drew et al., 2011; Kim and Kim, 2010), and is thought to reflect the passive mechanical properties of the vessel wall (Clark, 1933; Edvinsson et al., 1983). Theoretical models incorporating the fast arterial and slow venous components reproduce the observed cerebral hemodynamic response well (Barrett et al., 2012; Kim et al., 2013). However, there is spatial variation in HRFs across the brain (Aquino et al., 2014; Bießmann et al., 2012; Handwerker et al., 2004), which may underlie the diverse temporal profiles of hemodynamic responses across the entire cortex (Gonzalez-Castillo et al., 2012; Vickery et al., 2011).

The arterial and venous CBV changes induced by long sensory stimulation have different spatial extents (Kim and Kim, 2010), with the arterial component being more spatially restricted. This suggests that spatial variation (Handwerker et al., 2004) in HRFs might be due to differences in arterial and venous contributions to the HRF. Since the spatial pattern of the arterial response is thought to be more closely related to the spatial pattern of neural activity (Moon et al., 2013), brief, temporally isolated stimuli will give a hemodynamic response that more precisely reflects the underlying neural activity. However, using impulse-like stimuli is not always possible, particularly when using ‘naturalistic’ stimuli, which have multiple time-scales (Kay et al., 2008; Ben-Yakov et al., 2012; Honey et al., 2012; Naselaris et al., 2011). A method of separating the more localized arterial response from the less specific venous response to temporally extended stimuli would be very helpful for these stimulation paradigms.

Here, we investigated the vascular mechanisms underlying the hemodynamic response function in the superficial layers of the cortex in response to exercise. Previous work on the existence, localization and even direction of cerebral blood flow and volume changes during exercise are contentious (reviewed in (Ide and Secher, 2000)), with some studies showing no

changes (Globus et al., 1983), some showing global, non-specific increases (Herholz et al., 1987), and other showing localized increases (Jørgensen et al., 1992; Linkis et al., 1995). One explanation for the discrepancies among these studies, which use different methodologies and durations of exercise, is that different techniques have different sensitivity to arterial versus venous changes. We have previously shown, using intrinsic optical signal (IOS) imaging in head-fixed, voluntarily locomoting mice, that in the first few seconds of locomotion, the frontal cortex shows little to no change in blood volume, while there are substantial increases in blood volume in the limb representations of sensory cortex (Huo et al., 2014). Because arteries and veins have very different temporal (Kim and Kim, 2010; Drew et al., 2011; Gao and Drew, 2014) and spatial (Moon et al., 2013) dynamics, we wanted to determine if the discrepancies in the spatial extent of the hemodynamic response to exercise could be due to different spatial extents of arterial and venous changes.

Using two-photon laser scanning microscopy (2PLSM) (Drew et al., 2011; Shih et al., 2012), we measured individual vessel dilation dynamics during voluntary locomotion in awake, head-fixed mice (Dombeck et al., 2007; Nimmerjahn et al., 2009; Huo et al., 2014). Based on these single vessel measurements, we developed a HRF model to quantify the spatiotemporal characteristics of optically measured pixel-wise CBV changes in the superficial layers. We demonstrate that using the temporal dynamics of the blood volume signal, distinct spatial maps of the localized arterial and diffuse venous responses could be extracted. The arterial and venous responses to locomotion were linear, and repeatable across trials. Using our linear convolution model to separate the more spatially localized arterial changes from the less localized venous responses should prove useful for experiments using dynamic stimuli (Hasson et al., 2010).

A subset of the IOS data presented here has been previously presented (Huo et al., 2014), and is reanalyzed below.

Methods

Animals

All care and experimental manipulation of animals were done in accordance with the Institutional Animal Care and Use Committee of Pennsylvania State University, University Park. A total of 18 male C57BL/6J mice (Jackson Laboratory) were used. Mice were maintained on a 12-hour light/dark cycle in isolated cages.

Surgery

Mice were 2–10 months old (25–40 g) at the time of surgery. All surgical procedures were performed under isoflurane anesthesia. For 2PLSM imaging, polished and reinforced thinned-skull (PoRTS) windows were implanted (Drew et al., 2010; Shih et al., 2012; Gao and Drew, 2014) in the right parietal cortex (N=10). Under anesthesia, a custom-machined titanium head-bolt was attached to the skull and 3 self-tapping, 3/32" #000 (J.I. Morris) screws were implanted into the skull and connected to the head-bolt with dental cement. Using a hand drill (Foredome), the skull over the right parietal cortex was carefully thinned to ~30µm with a #7 bit (Fine Science Tools). It was then polished with 3f and 4f lapidary

polish (Convington Engineering, Redlands, CA, USA), and a #0 coverslip was attached to the skull with cyanoacrylate glue (Vibra-Tite, 32002). A meniscus-holding well was made with dental cement around the window. For IOS imaging, larger reinforced thinned-skull windows (Huo et al., 2014) that spanned frontal and parietal cortices were made either bilaterally (N=6) or unilaterally (N=2). For animals used for IOS imaging, the skull over frontal and parietal cortices in each hemisphere was thinned to remove skull vessels using a Foredom drill with the frontal-parietal suture sealed with cyanoacrylate glue and dental cement. Then the frontal-parietal suture was exposed and carefully thinned until the suture was flush with the frontal and parietal bones. Successful suture thinning was identified by absence of dural or pial vasculature remodeling after surgery. A #1 coverslip cut to the window size in each hemisphere was mounted using cyanoacrylate glue (Vibra-Tite, 32002). A custom machined titanium head-bolt was glued to the skull, centered on the midline suture, posterior to lambda. One self-tapping, 3/32" #000 (J.I. Morris) screw was implanted into the skull over the olfactory bulb and connected to the head-bolt via midline suture using cyanoacrylate glue and black dental acrylic resin (Lang Dental Mfg. Co., REF 1530) to minimize skull movement, and to absorb reflected light. Keeping the skull intact is important for accurate measures of hemodynamic signals, as craniotomies are known to cause inflammation (Cole et al., 2011; Xu et al., 2007), changes in brain tissue mechanical properties (Hatashita and Hoff, 1987), and angiogenesis (Arieli et al., 2002; Drew et al., 2010; Sohler et al., 1941), all of which are likely to disrupt the normal hemodynamic response.

Experiments

The treadmill (60 mm diameter) had one degree of freedom, and was covered with nonabrasive antislip tape. An optical rotary encoder (US Digital, E7PD-720-118) (Nimmerjahn et al., 2009) was attached to the treadmill axle to quantify the mouse's velocity. Mice were habituated to being head-fixed on the spherical treadmill over 3–5 days. All experiments were performed within 8 months of surgery in sound attenuating boxes.

Before each 2PLSM imaging session, the mouse was briefly anesthetized with isoflurane and infraorbitally injected with 50 μ L 5% (weight/volume) fluorescein conjugated dextran (70 kDa; Sigma-Aldrich). The two-photon microscope consists of a Sutter Movable Objective Microscope and a MaiTai HP laser, controlled by MPScan software (Nguyen et al., 2006). Images were acquired at 6–9 Hz for ~20 minutes/trial using water dipping objectives (Olympus, 10 \times 0.3 N.A. 20 \times 0.5 N.A., or 20 \times 1.0 N.A.). For imaging of pial vessels, power exiting the objective was typically 15–20 mW at 800 nm. We selected a rectangular field of view containing both arteries and veins (Fig. 2A). A total of 151 arteries and 104 veins in 10 mice were imaged.

IOS and laser Doppler flowmetry (LDF) data were collected using custom-written software in LabView 8.6 (National Instruments). For IOS imaging, four 530 nm LEDs (Thorlabs, M530L2-C1) (Bouchard et al., 2009) passed through a \pm 10 nm filter (Thorlabs, FB530-10) were used to uniformly illuminate the cortical surface. A CCD camera (Dalsa, Pantera 1M60) was used to acquire 12-bit images (Drew and Feldman, 2009). Each 256 \times 256 pixel image had a resolution of 27–37 μ m/pixel. A second camera (Microsoft, LifeCam Cinema)

was used to observe the mouse's behavior. After the animal was habituated, we collected IOS data at a frame rate of 3 Hz (~33 minutes/trial). In order to measure the power spectrum of the intrinsic signal (Fig. 1), some trials were collected at 30 Hz, but these were not used for fitting of the arterial and venous parameters due to the short duration of the trial (~3 minutes/trial).

For cerebral blood flow (CBF) measurements, an LDF optical probe (Oxford Optronix, OxyFlo) was placed at 30-degree angle to the window plane on the left hemisphere. When the LDF signal and IOS were recorded simultaneously, a 530 ± 5 nm filter was attached to the CCD camera to block light from the LDF probe.

At the conclusion of the experiments, mice were euthanized and the brain was processed for cytochrome oxidase staining (Drew and Feldman, 2007). The limb representations and barrels were aligned with the imaging windows using a combination of vascular images and fiduciary marks (Drew and Feldman, 2009). A polygon enclosing forelimb/hindlimb (FL/HL) representation was selected based on cytochrome oxidase staining (Fig. 1B).

Data Processing

All data analyses and statistical tests were performed in Matlab (MathWorks). To calculate baselines, about ten-second long periods were chosen in at the end of ~30 second period where there was no locomotion. This was long enough for the arterial and venous signal from any short running bouts preceding this period to become negligible.

For 2PLSM data, we removed artifacts from horizontal plane motion using frame-by-frame registration of the vessel images (Drew et al., 2011; Guizar-Sicairos et al., 2008). To quantify the diameter of a vessel, a rectangular box was manually drawn around a short segment (2–5 μm) of vessel (Fig. 2B). The pixel intensities were averaged along the long axis of the vessel, and the diameter, D , was calculated from the full width at half-maximum (Drew et al., 2011). Vessel diameter percentage changes, D/D_0 , were calculated by normalizing to the average diameter during a ~10-second period: $D/D_0 = (D - D_0)/D_0$. Time series of D/D_0 were first filtered with a three-point median filter, and then low-pass filtered (Butterworth) at 3 Hz.

For IOS images, regions of interest (ROIs) enclosing the thinned-skull windows were selected. Data taken on different days were registered off-line. A ~10 second period within a long period of rest was used to calculate the baseline IOS image, R_0 , for each day. The calculated fractional change of IOS from baseline, R/R_0 , was given by: $R/R_0 = (R - R_0)/R_0$. The R/R_0 data were mean-subtracted, and low-pass filtered at 1 Hz (Butterworth). We chose this cutoff frequency because it was adequate to capture the dynamics of the arterial response (see Supplementary Fig. S1).

For LDF data, we defined the baseline flux, Q_0 , by taking the average value of CBF during a ~10-second period when the animal was stationary. For all trials taken on the same day, we normalized all LDF data against this value to obtain fractional change of CBF, $Q/Q_0 = (Q - Q_0)/Q_0$. The Q/Q_0 data were mean-subtracted and low-pass filtered at 5 Hz (Butterworth).

Linear model

We constructed a linear convolution model to fit the observed changes in hemodynamic signals based on the assumption that the hemodynamic response to locomotion is a linear, time-invariant (LTI) system (Boynton et al., 1996; Cardoso et al., 2012; Glover, 1999; Vazquez and Noll, 1998). The input is the binarized locomotion signal. The output, or response, is any one of our hemodynamic measurements, including changes in diameter, D/D_0 from 2PLSM, changes in reflectance, R/R_0 from IOS, and changes in flux, Q/Q_0 from the LDF signal. The transfer function to individual locomotion event, or the impulse response function, is the hemodynamic response function (HRF). This model can be described as,

$$\frac{\Delta \vec{x}_{m \times 1}}{x_0} = \vec{s}_{m \times 1} * \vec{h}_{x, n \times 1} \quad (1)$$

where x is either the vessel diameter (D), the IOS signal (R), or the cerebral blood flow, Q , and consists of m data points. \vec{s} is a vector of the same length as \vec{x} that contains binary locomotion events, and \vec{h}_x is the measurement-specific HRF with n data points, where $n \ll m$.

To identify locomotion events, velocity was low-pass filtered at 10 Hz. Acceleration was calculated as the absolute value of the first derivative of the filtered velocity. The acceleration of the ball should be proportional to the force the paws experience, and thus closely related to the neural activity driven by the tactile sensory input. Acceleration was binarized according to the equation:

$$\delta(T) = H(a_T - a_c) = \begin{cases} 1, & \text{if } a_T \geq a_c; \\ 0, & \text{otherwise.} \end{cases} \quad (2)$$

where the threshold acceleration a_c was chosen at 1×10^{-6} m/s²; a_T is the instantaneous acceleration at time T , with a sampling rate of 30 kHz, and $H(\bullet)$ is the binary Heavyside function. We then converted the binarized acceleration signal, $\delta(T)$, to binary locomotion events, $s(t)$, at the same temporal resolution as the corresponding hemodynamic measurement. We set $s(t)$ to 1, representing a locomotion event, if at least 10% of $\delta(T)$ was 1 within the time spanned between each two consecutive IOS images. Otherwise $s(t) = 0$. (Huo et al., 2014)

For model fitting, all free parameters in the linear convolution models were estimated by minimizing the mean-squared error (MSE) between the experimental data and estimates of the linear convolution model using the MATLAB function *fminsearch*. In this algorithm, we performed unconstrained nonlinear optimization by iteratively search for the next best parameter until the improvement of MSE was below a tolerance threshold (1×10^{-8}) with a marginal change of parameter ($< 1 \times 10^{-8}$). The initial value of each parameter was fixed at 0.1 for all fittings, which was distant from the final fitted value.

We also solved directly for the kernel (HRF) numerically (Keesman, 2011). Writing the linear convolution model in matrix form, we had

$$X_{(m+n) \times 1} = T(\vec{s})_{(m+n) \times (n+1)} \times H_{(n+1) \times 1} \quad (3)$$

where $X_{(m+n) \times 1} = \begin{pmatrix} \Delta \vec{x}_{m \times 1} / x_0 \\ \vec{0}_{n \times 1} \end{pmatrix}$. $T(\vec{S})$ is a matrix containing the Toeplitz transformation of locomotion events \vec{S} :

$$T(\vec{s}) = \begin{pmatrix} 1 & s_1 & 0 & \cdots & 0 \\ 1 & s_2 & s_1 & \cdots & 0 \\ & & & \ddots & \\ \vdots & s_n & s_{n-1} & \cdots & s_1 \\ 1 & 0 & s_n & \cdots & s_2 \\ & & & \ddots & \\ 1 & 0 & 0 & \cdots & s_n \end{pmatrix} \cdot \quad (4)$$

The matrix T is real as it contains only binary data. T is full rank column-wise as long as \vec{S} is not empty, that is, there is at least one acceleration event above threshold. The vector \vec{H} containing the impulse response \vec{h}_x , $\vec{H} = \{0, \vec{h}_x\}^T$, where h_0 is a constant shift, can be solved as:

$$\vec{H} = (T^T T)^{-1} T^T X \quad (5)$$

To avoid boundary effects, we shifted the input \vec{S} forward by truncating the first 10 seconds of data (see Supplementary Fig. S3A, S3C).

In order to estimate the maximal change of hemodynamic signal, x_{max}/x_0 , we convolved the fitted or numerically solved HRF with a saturating stimulus, mimicking a long bout of locomotion, such that the simulated hemodynamic signal plateaued (see Supplementary Fig. S3B, S3D) at the value of x_{max}/x_0 .

Other than early exploratory studies, we did not attempt to fit the CBV HRF with a gamma distribution function (Boynton et al, 1996), as numerical calculations of the CBV locomotion-evoked HRF clearly showed a different profile from gamma distribution (see Supplementary Fig. S3). Numerically calculated HRFs were similar across animals.

All reported summary data were in the form of mean \pm standard deviation. All statistical tests using ‘‘ANOVA’’ were one-way ANOVA unless otherwise specified. Animal numbers were not predetermined, and all tests of statistical power were done *post hoc*.

Results

Spatiotemporal features of locomotion-driven changes in the intrinsic optical signal

We acquired the CBV-related intrinsic optical signal (IOS) in the dorsal frontal and parietal cortices of awake mice that were head-fixed on top of a spherical treadmill. Decreases in fractional reflectance from the baseline, R/R_0 , corresponded to increases in CBV (Malonek and Grinvald, 1996; Sirotin and Das, 2009). The hemodynamic response to locomotion had a characteristic multiphasic temporal profile (Fig. 1C). Following locomotion initiation, we observed a strong decrease in R/R_0 in the parietal cortex, especially the forelimb/hindlimb (FL/HL) representations in the primary sensory cortex (SI). At the conclusion of each locomotion event, R/R_0 initially recovered towards baseline rapidly, then with a slower time course, indicative of two distinct processes. For prolonged bouts of locomotion lasting tens of seconds or more, the decrease in R/R_0 in the parietal cortex could be >10%. However, there was little to no locomotion-driven changes in R/R_0 in the frontal cortex (Huo et al., 2014).

In order to accurately estimate the HRF, the input bandwidth must span the output bandwidth (Marmarelis and Marmarelis, 1978). This criterion was satisfied between the binarized locomotion power spectrum (the input) and the power spectrum of the average R/R_0 throughout the entire windows (the output) (Fig. 1D). In addition to the large, low frequency fluctuations in the reflectance signal driven by locomotion, there were small heart rate-induced fluctuations restricted to the frequency range of 8 – 12 Hz (Fig. 1D). Most locomotion events were brief (<1 s) (Fig. 1E). However, most of these short events are correlated in time (Fig. 1C), consistent with the large power at low frequencies in the power spectrum of binarized locomotion (Fig. 1D).

Dynamics of pial arterial and venous dilations

The fast and slow components of CBV increase in SI FL/HL areas measured with IOS (Fig. 1B) could be due to multiple time-scale behavior at the individual vessel level, or to heterogeneous response dynamics across vessel types (Blinder et al., 2013; Shih et al., 2012). To determine how individual vessel dynamics drive CBV changes during locomotion, we employed 2PLSM to visualize individual pial vessels (Drew et al., 2011; Shih et al., 2013) in the SI FL/HL representations of mice head-fixed on the treadmill (Fig. 2A). We focused on pial vessels because voluntary locomotion drives very small dilations of penetrating vessels (Gao, Greene, and Drew, *unpublished results*), which therefore are not likely to contribute substantially to changes in the intrinsic signal. During periods of quiescence, we observed spontaneous, low-frequency fluctuations in the diameters of pial arteries (Fig. 2C, < 20% peak-to-peak), consistent with measurements in stationary mice (Drew et al., 2011) and with measurements in the IOS (Huo et al., 2014), while pial veins exhibited very small changes in diameter (Fig. 2C).

The pial arteries dilated strongly and rapidly in response to both brief and prolonged voluntary locomotion events ($45.1\% \pm 26.7\%$ peak dilation). At the cessation of locomotion, the arteries constricted back to their baseline diameter within a few seconds (Fig. 2C). In contrast, dilations of pial veins were only apparent after longer bouts of locomotion due to

their smaller amplitudes ($15.4\% \pm 15.5\%$ peak dilation). The diameters of veins took tens of seconds to return to baseline (Fig. 2C). Locomotion-driven arterial and venous dilations were very similar in magnitude and time course to those evoked by vibrissae stimulation in stationary mice, and exhibited the same spontaneous dilations in the absence of overt sensory stimulation (Drew et al., 2011) (see Supplementary Fig. S1). However these dilations are substantially larger than those of vessels in anesthetized animals (Drew et al., 2010; Tian et al., 2011), consistent with the observation that anesthesia profoundly disrupts the activity of neurons (Chapin and Lin, 1984) and astrocytes (Thrane et al., 2012), making anesthesia more akin to a coma than reflecting normal brain function (Brown et al., 2010). The similarities of the vascular responses to passively presented sensory stimuli and to somatosensory stimulation that was actively generated suggested that the hemodynamic response was not affected by the behavioral state (locomoting vs. stationary) in the awake condition.

HRFs of pial vessel in response to voluntary locomotion

To quantify the relationship between individual vessel dilation and locomotion stimulus, we used a linear convolution model:

$$\frac{\Delta \vec{D}}{D_0} = \vec{s} * \vec{h}_D + c + \vec{e} \quad (6)$$

where \vec{D} is the time series of vessel diameter, D_0 is the baseline diameter at rest, \vec{s} is a vector of the binary locomotion events, c is a constant offset term, and \vec{e} is the vector of errors (assumed to be Gaussian) that is minimized in the fitting. We used binarized locomotion (thresholded absolute acceleration) because in initial experiments we found that the correlation between the hemodynamic signal and the binarized locomotion was stronger than between the hemodynamic signal and raw velocity (not shown). To characterize the dilation of an individual vessel in response to locomotion, we approximated the HRF, \vec{h}_D , as a decaying exponential function, where each vessel's behavior was described by its dilation amplitude (A_D) and time constant (τ_D) of recovery, such that at each time point t ,

$$h_D(t; A_D, \tau_D) = A_D e^{-t/\tau_D} \quad (7)$$

The dynamics of individual arteries and veins were well estimated with this model by fitting the parameters A_D , τ_D , and c to individual trials (Fig. 3) (Pearson's correlation coefficient, $cc = 0.62 \pm 0.16$ for arteries; $cc = 0.52 \pm 0.16$ for veins).

The fits for the time constants, τ_D , of arteries (5.5 ± 5.1 s) were significantly faster than those of veins (25.1 ± 17.9 s; ANOVA: $p < 0.001$) (Fig. 3A). The amplitudes, A_D , of arterial HRF ($10.8\% \pm 7.0\%$) were ~ 10 -fold larger than that of the veins ($0.9\% \pm 0.7\%$; ANOVA: $p < 0.001$). The maximal dilation, $A_{D,max}$, obtained by convolving with a simulated stimulus with long enough duration that it saturates the vessel dilatory response, was significantly larger in arteries ($33.9\% \pm 26.7\%$) than in veins ($16.8\% \pm 12.0\%$; ANOVA: $p < 0.001$). Similarly, in response to a single locomotion event, the total dilation integrated over time, $A_D \tau_D$, was significantly larger in arteries (5.57 ± 3.93 s) than in veins (2.61 ± 2.01 s);

ANOVA: $p < 0.001$) (Fig. 3B). Time constants, integrated areas and goodness-of-fit, measured by cc, were all consistent across animals (see Supplementary Fig. S2). Smaller arteries had larger dilation amplitudes (log linear regression, slope = $-0.02 \mu\text{m}^{-1}$, $p < 0.001$), whereas veins showed no size dependence of responses ($p > 0.05$), consistent with previous observations (Drew et al., 2011; Lee et al., 2001).

HRF of CBV-based intrinsic signal changes

Dilations of arteries and veins will increase local blood volume, decreasing reflectance in IOS. The correlation between locomotion and R/R_0 change in the parietal cortex was always significant (Pearson's correlation coefficient, t-test: $p < 0.001$), but not in the frontal cortex (t-test: $p > 0.05$), implying the linearity in the strongly responding parietal cortex. For each pixel, we fit the R/R_0 measurements in response to locomotion with a linear convolution model, similar to the one used for single vessels:

$$\frac{\Delta \vec{R}_i}{R_{i0}} = \vec{s} * \vec{h}_{R_i} + c_i + \vec{e}_i. \quad (8)$$

Here \vec{R}_i/\vec{R}_{i0} is the fractional change of reflectance from baseline of pixel i , c_i is a constant offset associated with pixel i , and \vec{e}_i is a time-varying error term that is minimized for each pixel during the fitting. We constrained the HRF of the i th pixel, \vec{h}_{R_i} , to be weighted sum of a fast arterial and slow venous component:

$$h_{R_i}(t; a_i, v_i) = a_i e^{-t/\tau_a} + v_i e^{-t/\tau_v}, \quad (9)$$

where fast decay time constant τ_a was fixed at 4 s, and slow decay τ_v at 40 s, based on our 2PLSM measurements. The pixel-specific weights, a_i and v_i , reflect the individual contributions of arteries and veins to blood volume increases within the area of the i th pixel. We assumed that any responses of capillaries were subsumed into one or both of these terms (Kim & Kim 2011; Hall et al. 2014). The values of a_i and v_i were fitted to the entire trial of each pixel (Fig. 4A). Due to its strong hemodynamic response to locomotion, the parietal cortex yielded a significantly higher average correlation between the fitted and actual responses (cc = 0.70 ± 0.07) than in the frontal cortex (cc = 0.40 ± 0.06 ; ANOVA: $p < 0.001$) (Fig. 4B, 5C). This model does not capture the ongoing, spontaneous fluctuation in the hemodynamic signal (Fox and Raichle, 2007; Mayhew et al., 1996; White et al., 2011), effectively setting an upper bound on the quality of our fit. HRFs directly calculated from binarized locomotion and changes in reflectance yielded a similar shape as our bi-exponential HRF construction (see Supplementary Fig. S3A), implying that our parametric simplification captured the essential features of the responses. We found that the exact values of time constants used for the arterial and venous component did not affect fit significantly, so long as they were well separated in value and both resided within the range of time constants for arterial and venous dilation, respectively, to capture the dynamics of the response. More complicated models, potentially including non-linearities, could improve upon the quality of the fits. Varying the time constants by 50% did not change the spatial pattern or the correlation of the fits (see Supplementary Fig. S4). The advantage of using the

simplified parameterized HRF is that both a_i and v_i , which have clear physical interpretations, could be visualized and analyzed independently from each other.

Differing spatial pattern of the arterial and venous responses

We then looked at the spatial patterns of the arterial and venous fitting parameters, a_i and v_i . The fit amplitude of a pixel will not only depend on the fractional change in CBV, but on the relative amount of blood volume in the pixel. The pixels containing large surface vessels will have a larger fractional blood volume than parenchymal pixels, and thus will be more prominent. We found that the patterns of arterial and venous weights consistently separated out the large vessels in the arterial and venous networks (Fig. 5A), with the pixels containing large arteries having large values of a_i , and pixels containing large veins having large values of v_i . The parenchyma exhibited a mixture of the arteries and veins due to the contribution of pial vessels that were smaller than a single pixel, signals from penetrating arterioles and ascending venules, and potentially capillaries (Hall et al., 2014; Stefanovic et al., 2008). Visualizing the spatial pattern of the component fit amplitudes revealed distinct arterial and venous ‘maps’, and that the arterial response to locomotion was more localized than the venous response (Fig. 5A). We quantified this localization by measuring the area of activation of the venous and arterial maps. We defined the area as the area greater than half of the 99%tile peak response. The size of the activation area was $4.2 \text{ mm}^2 \pm 1.9 \text{ mm}^2$ in the arterial map, significantly smaller than the $6.1 \text{ mm}^2 \pm 1.9 \text{ mm}^2$ in the venous map (ANOVA: $p < 0.05$; $N=8$) (Fig. 5B). The average window size was $12.9 \text{ mm}^2 \pm 1.7 \text{ mm}^2$. The power ($1-\beta$) of the ANOVA testing differences in spatial spread between arteries and veins was 0.95.

We quantified the relative changes in arterial and venous volumes in response to saturating stimulation from our fits. The fractional contribution of the arterial component was given by:

$$\sum_{i=1}^N \frac{a_{i,\max}}{a_{i,\max} + v_{i,\max}} \quad (10)$$

where N is the number of pixels in the area of interest (either the FL/HL representation or the entire window area) and i represents the pixel. Based on the construction of HRF (9), the maximum arterial (venous) contribution for each pixel $a_{i,\max}$ ($v_{i,\max}$) is given by:

$$a_{i,\max} = \frac{a_i}{1 - e^{-1/f_s \tau_a}} \quad (11)$$

where f_s is the frame rate at which the IOS is measured. The arterial and venous components of CBV response to locomotion had nearly equal magnitude (Fig. 5C) in the FL/HL representation (arterial $45.8\% \pm 13.6\%$; venous $54.2\% \pm 13.6\%$; ANOVA: $p > 0.05$, $N=8$). When we examined the relative contributions across the entire window area, the arterial contribution dropped to $32.0\% \pm 14.2\%$ (venous $68.0\% \pm 14.2\%$; ANOVA: $p < 0.01$, $N=8$) (Fig. 5C). This result was due to the regional ‘negative’ arterial contribution to CBV, as the fitted values of a_i in the frontal cortex were negative (Fig. 5A). These results show that even during prolonged bouts of locomotion, which probably drive venous distention to their

physiological limits, the arterial volume contribution to blood volume changes is large and cannot be assumed to be negligible, contrary to the assumptions underlying the balloon model of the BOLD signal (Buxton et al., 1998).

Repeatability and robustness of fit parameters

Since studies using fMRI have typically found hemodynamic responses to be unreliable across trials widely spaced in time (Bennett and Miller, 2010), it is important for us to determine if the changes we observed to relatively natural stimuli are robust across trials. We tested if the parameters fitted on one trial (within-trial fitting) could predict the hemodynamic response to locomotion on a different trial (cross-trial prediction). Voluntary locomotion trials on the same mouse were separated in time by 1 to 94 days (mean of 16 ± 12 days). The measured R/R_0 on one trial and predicted response using the parameters from a different trial were very similar (Fig. 6; also see Supplementary Fig. S5). The temporal dynamics of a single pixel (Fig. 6A) and the spatial specificity of the entire window (Fig. 6B) were both well predicted using the parameters fitted on a different trial. For all trials within an animal, we averaged all correlation coefficients between each cross-trial prediction and the measured data within the FL/HL representations. The fitting quality of cross-trial prediction was $89.3\% \pm 7.7\%$ of the fitting quality of within-trial estimates (Fig. 6C). The fitted model could also be used to decode locomotion patterns (see Supplementary Fig. S6). These results show that the CBV response to locomotion is spatially and temporally robust and repeatable.

HRF of cerebral blood flow response to locomotion

Since vessel dilation lowers vascular resistance and thus increases blood flow, we next quantified the relationship between locomotion and changes of CBF. We measured local CBF using LDF in the frontal and parietal cortices (Fig. 7A, also see Supplementary Fig. S7). Again we fit the CBF with a linear convolution model,

$$\frac{\Delta \vec{Q}}{Q_0} = \vec{s} * \vec{h}_Q + c + \vec{e}, \quad (12)$$

where \vec{Q}/Q_0 represents the fractional change of CBF from baseline, and \vec{h}_Q is the CBF HRF to locomotion. The HRF is approximated with an exponential kernel,

$$h_Q(t; A_Q, \tau_Q) = A_Q e^{-t/\tau_Q} \quad (13)$$

where the amplitude A_Q and time constant τ_Q , along with the constant term c , are free parameters. In the parietal cortex, the correlation coefficient between data and the fitted response was consistently high ($cc = 0.74 \pm 0.07$, $N=3$), showing that this linear model is a good estimation of the CBF response to locomotion. In the frontal cortex, the goodness-of-fit was poor due to the small CBF response (see Supplementary Fig. S7). Again we tested the robustness of CBF response to locomotion in the parietal cortex of each animal. We found that the goodness-of-fit of cross-trial predictions were not significantly different from the within-trial fitting (Fig. 7B). The time constant of the HRF relating CBF to locomotion

was slightly shorter than the time constant of arterial dilation (Fig. 7C) ($\tau_Q = 2.62 \pm 1.33$ s). These results indicate that the pial arterial dilation in response to locomotion drives a corresponding linear increase in CBF.

Discussion

Hemodynamic signals, such as changes in cerebral blood flow and volume, are several steps removed from the neural activity that drives them (Attwell et al., 2010; Buxton, 2012), and are shaped by the architecture of the vascular network (Gardner, 2010). For this reason it is critical both to have a quantitative description of the hemodynamic response function in order to better interpret observed hemodynamic signals, and to understand the mechanistic basis of the microscopic changes in the vasculature that generate the HRF. Here, we demonstrated that macroscopic blood volume-related hemodynamic response to voluntary locomotion, measured using IOS imaging, could be separated into arterial and venous components with distinct spatial patterns, and that these spatial patterns of HRFs were robust across time.

An important limitation of this study is that though our optical approach gives us a much higher spatial resolution laterally than magnetic-resonance based imaging techniques, our IOS measurements are from hemodynamic changes in the superficial layers, due to light scattering by brain tissue and absorbance by hemoglobin (Tian et al., 2011). This is an important caveat, as several studies have shown small, but significant, laminar differences in stimulus-evoked CBV increases (indicative of dilation), in anesthetized animals (Hirano et al., 2011; Kim & Kim, 2010; Polaowsky & Kim 2014). As the vessels in the deeper layers may respond differently than the pial vessels, it remains to be seen if the dynamics of vessels in deeper layers can be captured using a two-component linear model like the one presented here. Recent advances in non-linear microscopy imaging techniques (Kobat et al., 2009; Horton et al., 2013) should enable measurements of single-vessel dynamics throughout the depth of the cortex in the future.

Interestingly, the HRFs obtained here are similar to the CBV HRF measured in response to electrical stimulation in anesthetized rats (Silva et al., 2007; Hirano et al., 2011), and the dynamics in the visual cortex of anesthetized cats (Kim and Kim, 2010). The distinct fast and slow components of the HRFs are similar to those seen in individual arteries and veins of mice that are stationary, but awake (Drew et al., 2011). This suggests that the combined arterial/venous response to stimulation is a fundamental, invariant feature of the cerebral vascular system across many physiological states. Additionally, for stimuli lasting less than a few seconds, the arterial component of the change in CBV is larger than the venous component, which is important in understanding the physiological basis of the BOLD signal (Buxton, 2012; Kim et al., 2013). Our results cannot be directly compared to BOLD signal HRFs in humans because the BOLD signal reflects primarily venous oxygenation changes, not arterial dilation (Kim and Ogawa, 2012), and thus has different temporal dynamics. We did not explicitly model any capillary dilation, as it is not clear whether the capillary dilation takes place on the time scale of seconds (Hall et al., 2014) or tens of seconds (Stefanovic et al., 2008), slightly and passively in response to upstream arteriole dilation (Kornfield and Newman, 2014), or not at all (Fernandez-Klett et al., 2010; Drew et al., 2011). Due to the

light scattering properties of the brain (Tian et al., 2011) and laminar differences in vasculature (Tsai et al., 2009), the IOS from the parenchyma will contain a mix of capillary and large surface vessel signals. Our results show that the dynamics of parenchymal signals can be explained with a sum of arterial and venous signals, which implies that during voluntary locomotion, there is little dilation from capillaries and/or that the capillaries dilate with a mix of fast and slow dynamics that can be subsumed into the arterial and/or venous components.

A second insight obtained from our decomposition of the hemodynamic response into venous and arterial components is that the spatial pattern of the contributions of the components varied across the cortex. By fitting the HRFs in a location-dependent manner, we were able to determine that the spatial extent of the arterial component of the CBV was significantly smaller than the spatial extent of the venous component. This indicates that the 'point spread function' of the venous volume change is broader than that of the arterial component. This knowledge, coupled with reconstructions of the vasculature (Blinder et al., 2013; Weber et al., 2008), should help constrain models of blood flow dynamics in the cortex (Boas et al., 2008). By separating the changes in arterial and venous components of the CBV, we are able to show that voluntary exercise immediately induces localized arterial blood volume increase, followed by slow, diffuse venous blood volume increases. These results solve a long-standing issue as to how localized increases in cerebral blood flow and volume are during exercise, showing that diffuse spatial blood volume increases can follow prolonged bouts of locomotion. Additionally, because of the larger venous contribution at locations distant from the center of hemodynamic activation, these more remote areas will have a slower HRF, consistent with a model of a poroelastic brain interacting with a vascular network (Aquino et al., 2014).

The mean correlation coefficients between our fits and the data, which use a behavioral input, are comparable to those of the fMRI BOLD response in anesthetized monkeys, using neural activity as the input to the linear system (Logothetis, 2002). The tight relationship we observed between behavior and the hemodynamic signal is surprising for several reasons. First, awake mice, even at rest, have ongoing neural activity in the brain, which partially contributes to the spontaneous hemodynamic fluctuations we observed and could not account for with our model. Secondly, the locomotion stimulus is of variable duration, which means any temporal non-linearity will reduce the correlation between the data and the predicted response. Lastly, because the level of spontaneous neural activity is substantially higher in the awake animal, one might suspect the proportional change in activity evoked by stimulation, the modulation amplitude of the neural activity, to be lower than in the anesthetized animal (Fiser et al., 2004; Goard and Dan, 2009; Goense and Logothetis, 2008), which would be expected to lower the dynamic range of the locomotion-evoked cerebral hemodynamic signal. Despite all these potential effects that would compromise the correlation between behavior and the resulting hemodynamic signal, we still observed a highly linear cerebral hemodynamic response, suggesting that although the local 'average' neural activity measured using electrophysiology may be a poor indicator of changes in cerebral blood flow and volume (Devor et al., 2008; Sirotnin and Das, 2009; Huo et al., 2014), these hemodynamic changes are still precisely controlled.

The dilations we observed in the cortical surface arterioles, both in response to locomotion and spontaneously (Figs. 2 & S1), were approximately three to five times larger than those seen in anesthetized mice (Drew et al., 2011; Nizar et al., 2013). Our results build on a substantial body of work showing that anesthesia profoundly disrupts neurovascular coupling, neural metabolism and the hemodynamic responses. The seminal work of Martin and colleagues (Martin et al., 2002, 2006a, & 2006b) showed that there is an increase in the strength of neurovascular coupling, and the response to hypercapnia in awake relative to anesthetized rats. The dynamics of these responses are much faster in awake rats than in anesthetized rats. Recent work has found similar slowing and reductions of the hemodynamic responses by anesthesia in the vibrissae and visual cortices of mice (Drew et al., 2011; PISAURO et al., 2013). In addition to changes in the hemodynamic response, anesthesia severely disrupts brain metabolism. The anesthetic alpha-chloralose, widely used in neurovascular coupling studies, decreases glucose metabolism in the cortex by more than 50% relative to the awake state (Dudley et al., 1982), the same magnitude of metabolic decrease of found in vegetative coma patients relative to “locked-in” patients and healthy controls (Levy et al., 1987). The BOLD response is significantly larger in magnitude in awake monkeys than under anesthesia (Goense and Logothetis, 2008). Thus, the awake and anesthetized brains are in profoundly different states, making it problematic to use the results of anesthetized animal studies to interpret the result of human neuroimaging studies.

Although we did not make measurements of blood gases (Drew et al., 2011), the arterial dilation we observed here was unlikely to be caused by changes in CO₂ concentration in the blood for two reasons. Arterial dilations caused by hypercapnia take several minutes under un-physiologically high CO₂ levels to reach the magnitude we observed (Ngai and Winn, 1996), though exposure to high CO₂ in the awake animal can cause faster hemodynamic responses associated with neural desynchronization (Martin et al, 2006a), and the observed increases in blood flow, blood volume and arterial diameter all peaked within seconds of the onset of locomotion, with very similar amplitudes and dynamics as seen during responses to sensory stimulation of the vibrissae (Drew et al., 2011). Secondly, moderate exercise in rats, comparable to our voluntary locomotion paradigm, causes hypocapnia (Fregosi & Dempsey, 1984), which would tend to cause vasoconstriction, not the vasodilation we see here.

Empirical models of the HRF grounded in measurement of individual pial vessel dynamics allow the separation of cerebral hemodynamic signals into distinct vascular components. Particularly, the ability to separate well localized arterial changes from more diffuse venous signals should improve the resolution and accuracy in functional connectivity studies (Fox and Raichle, 2007), reconstructions of stimuli from cerebral hemodynamic signals (Naselaris et al., 2011), and in understanding the microvascular mechanisms of vascular malfunction associated with neurodegenerative diseases (Iadecola, 2013) and aging (D’Esposito et al., 2003).

Supplementary Material

Refer to Web version on PubMed Central for supplementary material.

Acknowledgments

This work was supported by an award from the American Heart Association, a Scholar Award from the McKnight Endowment Fund for Neuroscience, NS078168 and NS079737 from the NIH to PJD, and ARRA stimulus funds through NS070701.

We thank A. Vazquez for helpful discussions and N. Zhang and P. Blinder for comments on the manuscript.

Abbreviations

CBV	cerebral blood volume
CBF	cerebral blood flow
HRF	hemodynamic response function
IOS	intrinsic optical signal
2PLSM	two-photon laser scanning microscopy
LDF	laser Doppler flowmetry
LTl	linear, time-invariant
MSE	mean-squared error
cc	correlation coefficient
ROI	region of interest
FOV	field of view
FL	forelimb
HL	hindlimb

References

- Aquino KM, Robinson PA, Schira MM, Breakspear M. Deconvolution of neural dynamics from fMRI data using a spatiotemporal hemodynamic response function. *NeuroImage*. 2014; 94:203–215. [PubMed: 24632091]
- Arieli A, Grinvald A, Slovin H. Dural substitute for long-term imaging of cortical activity in behaving monkeys and its clinical implications. *J Neurosci Methods*. 2002; 114:119–133. [PubMed: 11856563]
- Armstrong DM, Drew T. Discharges of pyramidal tract and other motor cortical neurones during locomotion in the cat. *J Physiol (Lond)*. 1984; 346:471–495. [PubMed: 6699782]
- Attwell D, Buchan AM, Charkpak S, Lauritzen M, Macvicar BA, Newman EA. Glial and neuronal control of brain blood flow. *Nature*. 2010; 468:232–243. [PubMed: 21068832]
- Barrett MJP, Tawhai MH, Suresh V. Arteries dominate volume changes during brief functional hyperemia: Evidence from mathematical modelling. *NeuroImage*. 2012; 62:482–492. [PubMed: 22587899]
- Beloozerova IN, Sirota MG, Swadlow HA. Activity of different classes of neurons of the motor cortex during locomotion. *Journal of Neuroscience*. 2003; 23:1087–1097. [PubMed: 12574439]
- Ben-Yakov A, Honey CJ, Lerner Y, Hasson U. Loss of reliable temporal structure in event-related averaging of naturalistic stimuli. *NeuroImage*. 2012; 63:501–506. [PubMed: 22813575]
- Bennett CM, Miller MB. How reliable are the results from functional magnetic resonance imaging? *Annals of the New York Academy of Sciences*. 2010; 1191:133–155. [PubMed: 20392279]

- Bießmann F, Murayama Y, Logothetis NK, Müller KR, Meinecke FC. Improved decoding of neural activity from fMRI signals using non-separable spatiotemporal deconvolutions. *NeuroImage*. 2012; 61:1-31-1042. [PubMed: 22401757]
- Blinder P, Tsai PS, Kaufhold JP, Knutsen PM, Suhl H, Kleinfeld D. The cortical angiome: an interconnected vascular network with noncolumnar patterns of blood flow. *Nat Neurosci*. 2013; 16:889–897. [PubMed: 23749145]
- Brown EN, Lydic R, Schiff ND. General anesthesia, sleep, and coma. *N Engl J Med*. 2010; 363:2638–2650. [PubMed: 21190458]
- Boas DA, Jones SR, Devor A, Huppert TJ, Dale AM. A vascular anatomical network model of the spatio-temporal response to brain activation. *NeuroImage*. 2008; 40:1116–1129. [PubMed: 18289880]
- Bouchard MB, Chen BR, Burgess SA, Hillman EMC. Ultra-fast multispectral optical imaging of cortical oxygenation, blood flow, and intracellular calcium dynamics. *Opt Express*. 2009; 17:15670–15678. [PubMed: 19724566]
- Boynton GM, Engel SA, Glover GH, Heeger DJ. Linear systems analysis of functional magnetic resonance imaging in human V1. *J Neurosci*. 1996; 16:4207–4221. [PubMed: 8753882]
- Buxton R, Wong E, Frank L. Dynamics of blood flow and oxygenation changes during brain activation: the balloon model. *Magn Reson Med*. 1998; 39:855–864. [PubMed: 9621908]
- Buxton RB. Dynamic models of BOLD contrast. *NeuroImage*. 2012; 62:953–962. [PubMed: 22245339]
- Cardoso MMB, Sirotin YB, Lima B, Glushenkova E, Das A. The neuroimaging signal is a linear sum of neurally distinct stimulus- and task-related components. *Nat Neurosci*. 2012; 15:1298–1306. [PubMed: 22842146]
- Chapin J, Woodward D. Modulation of sensory responsiveness of single somatosensory cortical cells during movement and arousal behaviors. *Experimental Neurology*. 1981; 72:164–178. [PubMed: 7202621]
- Chapin J, Lin C. Mapping the body representation in the SI cortex of anesthetized and awake rats. *J Comp Neurol*. 1984; 229:199–213. [PubMed: 6438190]
- Clark JH. The elasticity of veins. *Am J Physiol*. 1933; 105:418–427.
- Cole JT, Yarnell A, Kean WS, Gold E, Lewis B, Ren M, McMullen DC, Jacobowitz DM, Pollard HB, O'Neill JT. Craniotomy: True Sham for Traumatic Brain Injury, or a Sham of a Sham? *Journal of Neurotrauma*. 2011; 28:359–369. [PubMed: 21190398]
- D'Esposito M, Deouell LY, Gazzaley A. Alterations in the BOLD fMRI signal with ageing and disease: a challenge for neuroimaging. *Nat Rev Neurosci*. 2003; 4:863–872. [PubMed: 14595398]
- Devor A, Hillman EMC, Tian P, Waeber C, Teng IC, Ruvinskaya L, Shalinsky MH, Zhu H, Haslinger RH, Narayanan SN, Ulbert I, Dunn AK, Lo EH, Rosen BR, Dale AM, Kleinfeld D, Boas DA. Stimulus-induced changes in blood flow and 2-deoxyglucose uptake dissociate in ipsilateral somatosensory cortex. *Journal of Neuroscience*. 2008; 28:14347–14357. [PubMed: 19118167]
- Dombeck DA, Graziano MS, Tank DW. Functional Clustering of Neurons in Motor Cortex Determined by Cellular Resolution Imaging in Awake Behaving Mice. *Journal of Neuroscience*. 2009; 29:13751–13760. [PubMed: 19889987]
- Dombeck DA, Khabbaz AN, Collman F, Adelman TL, Tank DW. Imaging large-scale neural activity with cellular resolution in awake, mobile mice. *Neuron*. 2007; 56:43–57. [PubMed: 17920014]
- Dudley RE, Nelson SR, Samson F. Influence of chloralose on brain regional glucose utilization. *Brain Res*. 1982; 233:173–180. [PubMed: 7059799]
- Drew PJ, Feldman DE. Representation of moving wavefronts of whisker deflection in rat somatosensory cortex. *J Neurophysiol*. 2007; 98:1566–1580. [PubMed: 17567777]
- Drew PJ, Feldman DE. Intrinsic signal imaging of deprivation-induced contraction of whisker representations in rat somatosensory cortex. *Cerebral Cortex*. 2009; 19:331–348. [PubMed: 18515797]
- Drew PJ, Shih AY, Driscoll JD, Knutsen PM, Blinder P, Davalos D, Akassoglou K, Tsai PS, Kleinfeld D. Chronic optical access through a polished and reinforced thinned skull. *Nat Meth*. 2010; 7:981–984.

- Drew PJ, Shih AY, Kleinfeld D. Fluctuating and sensory-induced vasodynamics in rodent cortex extend arteriole capacity. *Proceedings of the National Academy of Sciences*. 2011; 108:8473–8478.
- Edvinsson L, Högestätt ED, Uddman R, Auer LM. Cerebral veins: fluorescence histochemistry, electron microscopy, and in vitro reactivity. *J Cereb Blood Flow Metab*. 1983; 3:226–230. [PubMed: 6841470]
- Fernandez-Klett F, Offenhauser N, Dirnagl U, Priller J, Lindauer U. Pericytes in capillaries are contractile in vivo, but arterioles mediate functional hyperemia in the mouse brain. *Proceedings of the National Academy of Sciences*. 2010; 107:22290–5.
- Fiser J, Chiu C, Weliky M. Small modulation of ongoing cortical dynamics by sensory input during natural vision. *Nature*. 2004; 431:573–578. [PubMed: 15457262]
- Fox MD, Raichle ME. Spontaneous fluctuations in brain activity observed with functional magnetic resonance imaging. *Nat Rev Neurosci*. 2007; 8:700–711. [PubMed: 17704812]
- Fregosi RF, Dempsey JA. Arterial blood acid-base regulation during exercise in rats. *J Appl Physiol Respir Environ Exerc Physiol*. 1984; 57:396–402. [PubMed: 6469809]
- Friston K, Jezzard P. Analysis of functional MRI time-series. *Hum Brain Mapp*. 1994; 1:153–171.
- Gardner JL. Is cortical vasculature functionally organized? *NeuroImage*. 2010; 49:1953–1956. [PubMed: 19596071]
- Gao Y-R, Drew PJ. Determination of vessel cross-sectional area by thresholding in Radon space. *J Cereb Blood Flow Metab*. 2014; 34:1180–1187. [PubMed: 24736890]
- Globus M, Melamed E, Keren A, Tzivoni D, Granot C, Lavy S, Stern S. Effect of exercise on cerebral circulation. *J Cereb Blood Flow Metab*. 1983; 3:287–290. [PubMed: 6409908]
- Glover G. Deconvolution of impulse response in event-related BOLD fMRI. *NeuroImage*. 1999; 9:416–429. [PubMed: 10191170]
- Goad M, Dan Y. Basal forebrain activation enhances cortical coding of natural scenes. *Nat Neurosci*. 2009; 12:1444–1449. [PubMed: 19801988]
- Goense JBM, Logothetis NK. Neurophysiology of the BOLD fMRI signal in awake monkeys. *Curr Biol*. 2008; 18:631–640. [PubMed: 18439825]
- Gonzalez-Castillo J, Saad ZS, Handwerker DA, Inati SJ, Brenowitz N, Bandettini PA. Whole-brain, time-locked activation with simple tasks revealed using massive averaging and model-free analysis. *Proceedings of the National Academy of Sciences*. 2012; 109:5487–5492.
- Guizar-Sicairos M, Thurman S, Fienup J. Efficient subpixel image registration algorithms. *Opt Lett*. 2008; 33:156–158. [PubMed: 18197224]
- Hall CN, Reynell C, Gesslein B, Hamilton NB, Mishra A, Sutherland BA, O’Farrell FM, Buchan AM, Lauritzen M, Attwell D. Capillary pericytes regulate cerebral blood flow in health and disease. *Nature*. 2014; 508:55–60. [PubMed: 24670647]
- Handwerker DA, Ollinger JM, D’Esposito M. Variation of BOLD hemodynamic responses across subjects and brain regions and their effects on statistical analyses. *NeuroImage*. 2004; 21:1639–1651. [PubMed: 15050587]
- Hasson U, Malach R, Heeger DJ. Reliability of cortical activity during natural stimulation. *Trends Cogn Sci (Regul Ed)*. 2010; 14:40–48. [PubMed: 20004608]
- Hatashita S, Hoff JT. The effect of craniectomy on the biomechanics of normal brain. *J Neurosurg*. 1987; 67:573–578. [PubMed: 3655895]
- Herholz K, Buskies W, Rist M, Pawlik G, Hollmann W, Heiss WD. Regional cerebral blood flow in man at rest and during exercise. *J Neurol*. 1987; 234:9–13. [PubMed: 3102697]
- Hillman EMC, Devor A, Bouchard MB, Dunn AK, Krauss GW, Skoch J, Bacskaï BJ, Dale AM, Boas DA. Depth-resolved optical imaging and microscopy of vascular compartment dynamics during somatosensory stimulation. *NeuroImage*. 2007; 35:89–104. [PubMed: 17222567]
- Hirano Y, Stefanovic B, Silva AC. Spatiotemporal Evolution of the Functional Magnetic Resonance Imaging Response to Ultrashort Stimuli. *Journal of Neuroscience*. 2011; 31:1440–1447. [PubMed: 21273428]

- Honey CJ, Thesen T, Donner TH, Silbert LJ, Carlson CE, Devinsky O, Doyle WK, Rubin N, Heeger DJ, Hasson U. Slow Cortical Dynamics and the Accumulation of Information over Long Timescales. *Neuron*. 2012; 76:423–434. [PubMed: 23083743]
- Horton NG, Wang K, Kobat D, Clark CG, Wise FW, Schaffer CB, Xu C. In vivo three-photon microscopy of subcortical structures within an intact mouse brain. *Nature Photonics*. 2013; 7:205–209.
- Huo BX, Smith JB, Drew PJ. Neurovascular Coupling and Decoupling in the Cortex during Voluntary Locomotion. *Journal of Neuroscience*. 2014; 34:10975–10981. [PubMed: 25122897]
- Iadecola C. The Pathobiology of Vascular Dementia. *Neuron*. 2013; 80:844–866. [PubMed: 24267647]
- Ide K, Secher NH. Cerebral blood flow and metabolism during exercise. *Progress in Neurobiology*. 2000; 61:397–414. [PubMed: 10727781]
- Joyner MJ, Wilkins BW. Exercise hyperaemia: is anything obligatory but the hyperaemia? *J Physiol (Lond)*. 2007; 583:855–860. [PubMed: 17640934]
- Jørgensen LG, Perko G, Secher NH. Regional cerebral artery mean flow velocity and blood flow during dynamic exercise in humans. *J Appl Physiol*. 1992; 73:1825–1830. [PubMed: 1474058]
- Kay KN, Naselaris T, Prenger RJ, Gallant JL. Identifying natural images from human brain activity. *Nature*. 2008; 452:352–355. [PubMed: 18322462]
- Keesman, KJ. *System Identification*. Springer; 2011.
- Kim JH, Khan R, Thompson JK, Ress D. Model of the transient neurovascular response based on promptarterial dilation. *J Cereb Blood Flow Metab*. 2013; 33:1429–1439. [PubMed: 23756690]
- Kim T, Hendrich KS, Masamoto K, Kim SG. Arterial versus total blood volume changes during neural activity-induced cerebral blood flow change: implication for BOLD fMRI. *J Cereb Blood Flow Metab*. 2007; 27:1235–1247. [PubMed: 17180136]
- Kim T, Kim S. Cortical layer-dependent arterial blood volume changes: improved spatial specificity relative to BOLD fMRI. *NeuroImage*. 2010; 49:1340–1349. [PubMed: 19800013]
- Kim T, Kim SG. Temporal dynamics and spatial specificity of arterial and venous blood volume changes during visual stimulation: implication for BOLD quantification. *J Cereb Blood Flow Metab*. 2010; 31:1211–1222. [PubMed: 21179068]
- Kim T, Kim S-G. Quantitative MRI of cerebral arterial blood volume. *Open Neuroimag J*. 2011; 5:136–145. [PubMed: 22253654]
- Kleinfeld D, Mitra P, Helmchen F, Denk W. Fluctuations and stimulus-induced changes in blood flow observed in individual capillaries in layers 2 through 4 of rat neocortex. *Proc Natl Acad Sci USA*. 1998; 95:15741. [PubMed: 9861040]
- Kobat D, Durst ME, Nishimura N, Wong AW, Schaffer CB, Xu C. Deep tissue multiphoton microscopy using longer wavelength excitation. *Opt Express*. 2009; 17:13354–13364. [PubMed: 19654740]
- Kornfield TE, Newman EA. Regulation of blood flow in the retinal trilaminar vascular network. *Journal of Neuroscience*. 2014; 34:11504–11513. [PubMed: 25143628]
- Lee S, Duong T, Yang G, Iadecola C, Kim S. Relative changes of cerebral arterial and venous blood volumes during increased cerebral blood flow: implications for BOLD fMRI. *Magn Reson Med*. 2001; 45:791–800. [PubMed: 11323805]
- Levy DE, Sidtis JJ, Rottenberg DA, Jarden JO, Strother SC, Dhawan V, Ginos JZ, Tramo MJ, Evans AC, Plum F. Differences in cerebral blood flow and glucose utilization in vegetative versus locked-in patients. *Ann Neurol*. 1987; 22:673–682. [PubMed: 3501694]
- Linkis P, Jørgensen LG, Olesen HL, Madsen PL, Lassen NA, Secher NH. Dynamic exercise enhances regional cerebral artery mean flow velocity. *J Appl Physiol*. 1995; 78:12–16. [PubMed: 7713801]
- Logothetis N. What we can do and what we cannot do with fMRI. *Nature*. 2008; 453:869–878. [PubMed: 18548064]
- Logothetis N, Pauls J, Augath M, Trinath T, Oeltermann A. Neurophysiological investigation of the basis of the fMRI signal. *Nature*. 2001; 412:150–157. [PubMed: 11449264]

- Logothetis NK. The neural basis of the blood-oxygen-level-dependent functional magnetic resonance imaging signal. *Philosophical Transactions of the Royal Society B: Biological Sciences*. 2002; 357:1003–1037.
- Malonek D, Grinvald A. Interactions between electrical activity and cortical microcirculation revealed by imaging spectroscopy: implications for functional brain mapping. *Science*. 1996; 272:551–554. [PubMed: 8614805]
- marmarelis, PZ.; Marmarelis, VZ. *Analysis of physiological systems: the white-noise approach*. Plenum Press; 1978.
- Martin C, Jones M, Martindale J, Mayhew J. Haemodynamic and neural responses to hyper-capnia in the awake rat. *European Journal of Neuroscience*. 2006a; 24:2601–2610. [PubMed: 17100848]
- Martin C, Martindale J, Berwick J, Mayhew J. Investigating neural-hemodynamic coupling and the hemodynamic response function in the awake rat. *NeuroImage*. 2006b; 32:33–48. [PubMed: 16725349]
- Martin C, Berwick J, Johnston D, Zheng Y, Martindale J, Port M, Redgrave P, Mayhew J. Optical imaging spectroscopy in the unanaesthetised rat. *J Neurosci Methods*. 2002; 120:25–34. [PubMed: 12351204]
- Martindale J, Mayhew J, Berwick J, Jones M, Martin C, Johnston D, Redgrave P, Zheng Y. The Hemodynamic Impulse Response to a Single Neural Event. *J Cereb Blood Flow Metab*. 2003:546–555. [PubMed: 12771569]
- Mayhew JE, Askew S, Zheng Y, Porrill J, Westby GW, Redgrave P, Rector DM, Harper RM. Cerebral vasomotion: a 0.1-Hz oscillation in reflected light imaging of neural activity. *NeuroImage*. 1996; 4:183–193. [PubMed: 9345508]
- Moon CH, Fukuda M, Kim SG. Spatiotemporal characteristics and vascular sources of neural-specific and -nonspecific fMRI signals at submillimeter columnar resolution. *NeuroImage*. 2013; 64:91–103. [PubMed: 22960251]
- Naselaris T, Kay KN, Nishimoto S, Gallant JL. Encoding and decoding in fMRI. *NeuroImage*. 2011; 56:400–410. [PubMed: 20691790]
- Ngai AC, Winn HR. Estimation of shear and flow rates in pial arterioles during somatosensory stimulation. *Am J Physiol*. 1996; 270:H1712–7. [PubMed: 8928878]
- Nguyen QT, Tsai PS, Kleinfeld D. MPScope: a versatile software suite for multiphoton microscopy. *J Neurosci Methods*. 2006; 156:351–359. [PubMed: 16621010]
- Nimmerjahn A, Mukamel EA, Schnitzer MJ. Motor Behavior Activates Bergmann Glial Networks. *Neuron*. 2009; 62:400–412. [PubMed: 19447095]
- Pisauro MA, Dhruv NT, Carandini M, Benucci A. Fast Hemodynamic Responses in the Visual Cortex of the Awake Mouse. *Journal of Neuroscience*. 2013; 33:18343–18351. [PubMed: 24227743]
- Poplawsky AJ, Kim SG. Layer-dependent BOLD and CBV-weighted fMRI responses in the rat olfactory bulb. *NeuroImage*. 2014; 91:237–251. [PubMed: 24418506]
- Shih AY, Blinder P, Tsai PS, Friedman B, Stanley G, Lyden PD, Kleinfeld D. The smallest stroke: occlusion of one penetrating vessel leads to infarction and a cognitive deficit. *Nat Neurosci*. 2013; 16:55–63. [PubMed: 23242312]
- Shih AY, Mateo C, Drew PJ, Tsai PS, Kleinfeld D. A polished and reinforced thinned-skull window for long-term imaging of the mouse brain. *J Vis Exp*. 2012:10.3791/3742
- Shih AY, Driscoll JD, Drew PJ, Nishimura N, Schaffer CB, Kleinfeld D. Two-photon microscopy as a tool to study blood flow and neurovascular coupling in the rodent brain. *J Cereb Blood Flow Metab*. 2012; 32:1277–1309. [PubMed: 22293983]
- Silva AC, Koretsky AP, Duyn JH. Functional MRI impulse response for BOLD and CBV contrast in rat somatosensory cortex. *Magn Reson Med*. 2007; 57:1110–1118. [PubMed: 17534912]
- Sirotnin YB, Das A. Anticipatory haemodynamic signals in sensory cortex not predicted by local neuronal activity. *Nature*. 2009; 457:475–479. [PubMed: 19158795]
- Sohler TP, Lothrop GN, Forbes HS. The pial circulation of normal, non-anesthetized animals part 1. Description of a method of observation. *Journal of Pharmacology and Experimental Therapeutics*. 1941; 71:325–330.

- Stefanovic B, Hutchinson E, Yakovleva V, Schram V, Russell JT, Belluscio L, Koretsky AP, Silva AC. Functional reactivity of cerebral capillaries. *J Cereb Blood Flow Metab.* 2008; 28:961–972. [PubMed: 18059431]
- Thrane AS, Thrane VR, Zeppenfeld D, Lou N, Xu Q, Nagelhus EA, Nedergaard M. General anesthesia selectively disrupts astrocyte calcium signaling in the awake mouse cortex. *Proc Natl Acad Sci USA.* 2012; 109:18974–18979. [PubMed: 23112168]
- Tian P, Teng IC, May LD, Kurz R, Lu K, Scadeng M, Hillman EMC, De Crespigny AJ, D'Arceuil HE, Mandeville JB, Marota JJA, Rosen BR, Liu TT, Boas DA, Buxton RB, Dale AM, Devor A. Cortical depth-specific microvascular dilation underlies laminar differences in blood oxygenation level-dependent functional MRI signal. *Proceedings of the National Academy of Sciences.* 2010; 107:15246–15251.
- Tian P, Devor A, Sakadžić S, Dale AM, Boas DA. Monte Carlo simulation of the spatial resolution and depth sensitivity of two-dimensional optical imaging of the brain. *J Biomed Opt.* 2011; 16:016006. [PubMed: 21280912]
- Tsai PS, Kaufhold JP, Blinder P, Friedman B, Drew PJ, Karten HJ, Lyden PD, Kleinfeld D. Correlations of neuronal and microvascular densities in murine cortex revealed by direct counting and colocalization of nuclei and vessels. *Journal of Neuroscience.* 2009; 29:14553–14570. [PubMed: 19923289]
- Vazquez AL, Noll DC. Nonlinear aspects of the BOLD response in functional MRI. *NeuroImage.* 1998; 7:108–118. [PubMed: 9558643]
- Vickery TJ, Chun MM, Lee D. Ubiquity and Specificity of Reinforcement Signals throughout the Human Brain. *Neuron.* 2011; 72:166–177. [PubMed: 21982377]
- Weber B, Keller AL, Reichold J, Logothetis NK. The Microvascular System of the Striate and Extrastriate Visual Cortex of the Macaque. *Cerebral Cortex.* 2008; 18:2318–2330. [PubMed: 18222935]
- White BR, Bauer AQ, Snyder AZ, Schlaggar BL, Lee JM, Culver JP. Imaging of Functional Connectivity in the Mouse Brain. *PLoS ONE.* 2011; 6:e16322. [PubMed: 21283729]
- Xu HT, Pan F, Yang G, Gan WB. Choice of cranial window type for in vivo imaging affects dendritic spine turnover in the cortex. *Nat Neurosci.* 2007; 10:549–551. [PubMed: 17417634]

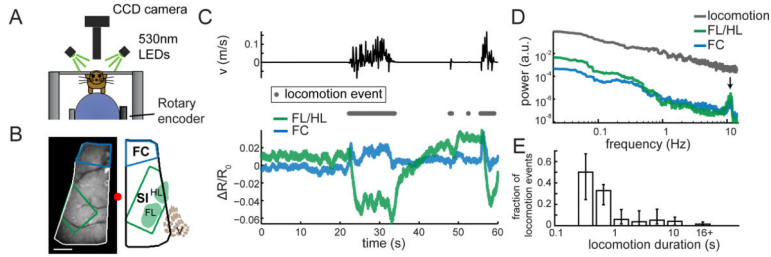


Figure 1. Cortical CBV responses show region-specific dynamics during locomotion
(A) Experiment setup for IOS imaging. The head-fixed mouse was free to run on a spherical treadmill with one degree of freedom. The cortex of the mouse was illuminated with 530nm light. **(B)** IOS image of cortex revealed in the thinned-skull window (*left*). Body representations in the primary somatosensory cortex (SI) and surrounding areas within the window (*right*) were identified with cytochrome oxidase staining. FC: frontal cortex; FL: forelimb; HL: hindlimb; V: vibrissae. Scale bar = 1 mm. **(C)** The ball velocity during 60-second trial of voluntary locomotion was recorded with rotary encoder (*top*), and then converted to binary locomotion events (*middle*). The average fractional changes of reflectance, R/R_0 (*bottom*), from the FL/HL representation (enclosed by green polygons in (B)) and FC (enclosed in blue contours in (B)), are plotted within this period, demonstrating the localized response. **(D)** Power spectrum density (PSD) plots of locomotion events (*gray*) and averaged R/R_0 in FL/HL area (*green*) and FC (*blue*). Arrow denotes heart-rate related oscillations. **(E)** Fraction of continuous locomotion events at different durations. The height of each bar represents the mean across animals. Error bars show the minimum (lower limit) and the maximum (upper limit) across all animals. N = 8 mice.

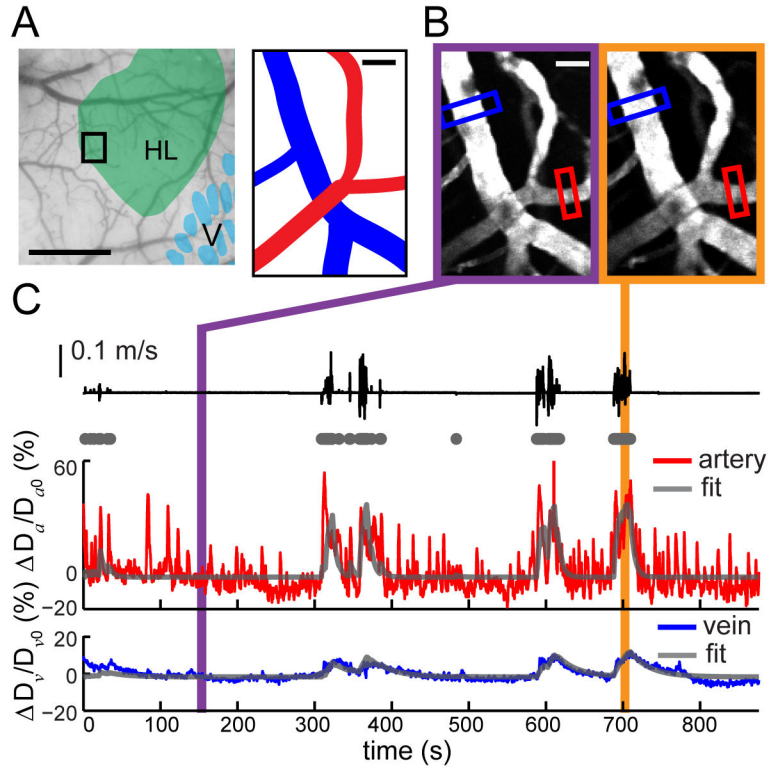


Figure 2. Locomotion-driven pial vessel dilations can be fitted with a linear model
(A) *Left*: Histologically identified hindlimb (*green*) overlaid on an image of a PoRTS window. Scale bar = 0.5 mm. 2PLSM FOV is enclosed in the black rectangle. *Right*: schematic depicts of an artery (red) and a vein (blue) from FOV. Scale bar = 20 μm . **(B)** Examples of 1-second average image of FOV under 2PLSM when the animal was at rest (*left*) and during locomotion (*right*). Diameter changes of the artery and the vein were recorded from the vessel segments within red and blue rectangular ROIs, respectively. Scale bar = 20 μm . **(C)** During voluntary locomotion (*black trace*), fractional change of diameters of the artery (D_a/D_{a0} , *red*) and the vein (D_v/D_{v0} , *blue*) shown in **(B)**. Using binarized locomotion events (*gray dots*) as inputs, each diameter was fitted with a linear model (*gray trace*). The correlation coefficient between the fits and the actual vessel response was 0.83 for the artery and 0.57 for the vein.

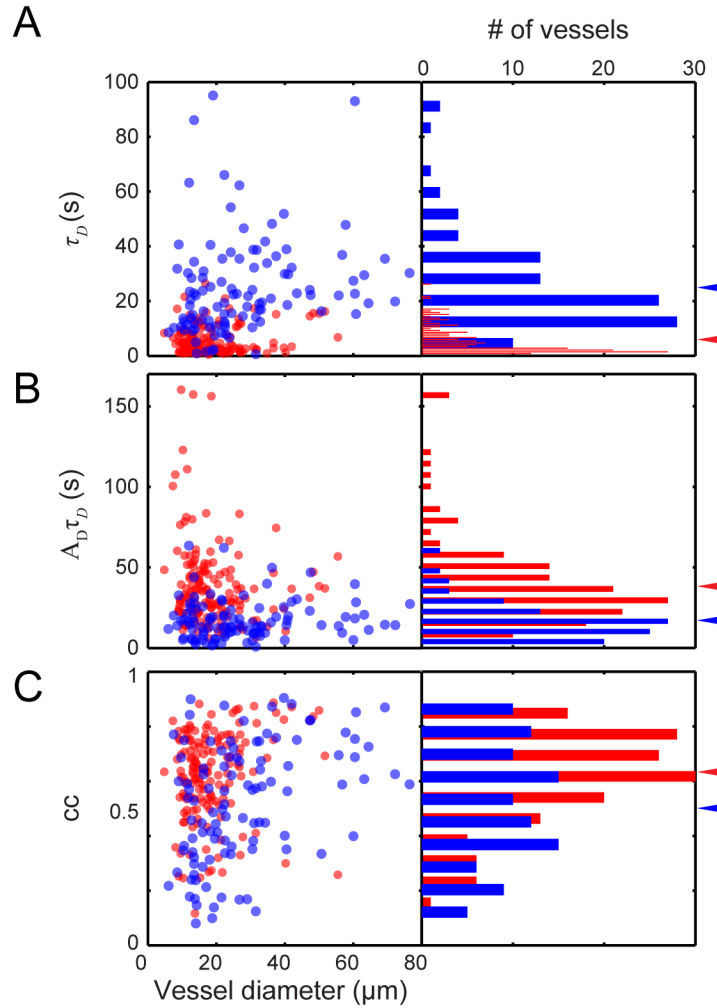


Figure 3. Quantification of time courses and amplitudes of responses of pial arteries and veins to locomotion using a linear model reveals distinct dynamics

(A) Fitted time constants (τ_D) of vessel recovery from dilation were significantly smaller for arteries (*red*) than for veins (*blue*) (ANOVA: $p < 0.001$). Red and blue arrowheads indicate the mean of for arteries (5.5 ± 5.1 s) and veins (25.1 ± 17.9 s), respectively. (B) Values of integrated areas of the estimated impulse response showed larger arterial (5.57 ± 3.93 s⁻¹, *red*) than venous (2.61 ± 2.01 s⁻¹, *blue*) diameter changes (ANOVA: $p < 0.001$). (C) Correlation coefficients (cc) between the data and model fitting for arteries (0.62 ± 0.16) and veins (0.52 ± 0.16) were similar across vessel diameters. Data from a total of 151 arteries and 104 veins were included in each plot.

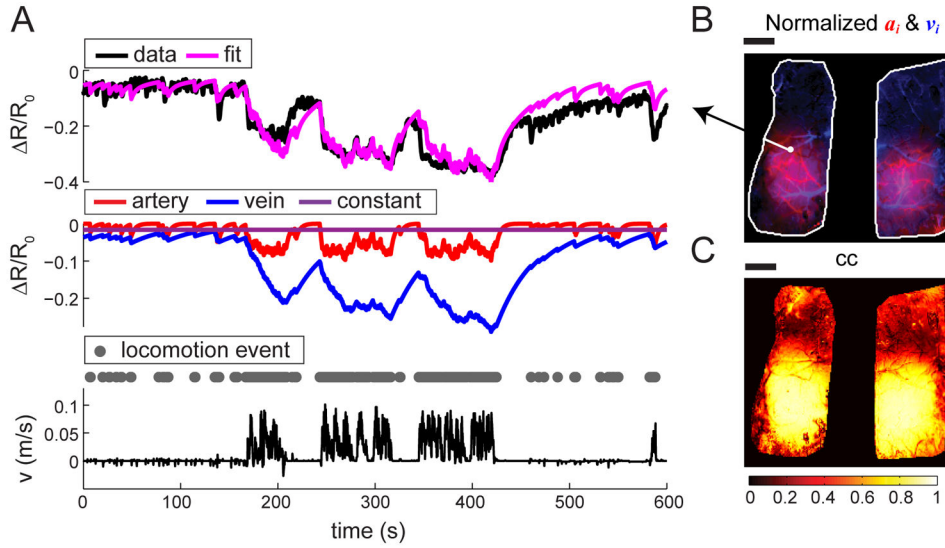


Figure 4. Linear convolution model captures the temporal dynamics of CBV response to locomotion

(A) *Top*: Example of pixel-wise model fitting. For a sample pixel signified in (B), we fitted the time series of R/R_0 (*top black*) with a linear convolution model (*magenta*; $cc = 0.83$). *Middle*: The model consisted of two dynamic components, a fast arterial (*red*) and a slow venous (*blue*) component, and a constant offset (*purple*). *Bottom*: Binary locomotion events (*gray dots*) were derived from recorded locomotion velocity (*black*). (B) Amplitude of the fast component, a_i (*red*), and amplitude of the slow component, v_i (*blue*), for all pixels within the ROI (*white outline*). (C) Correlation coefficients (cc) between the R/R_0 data and the fitted data of all pixels within the ROI. The correlation was highest in the regions with largest decrease in reflectance. Scale bars: 1 mm.

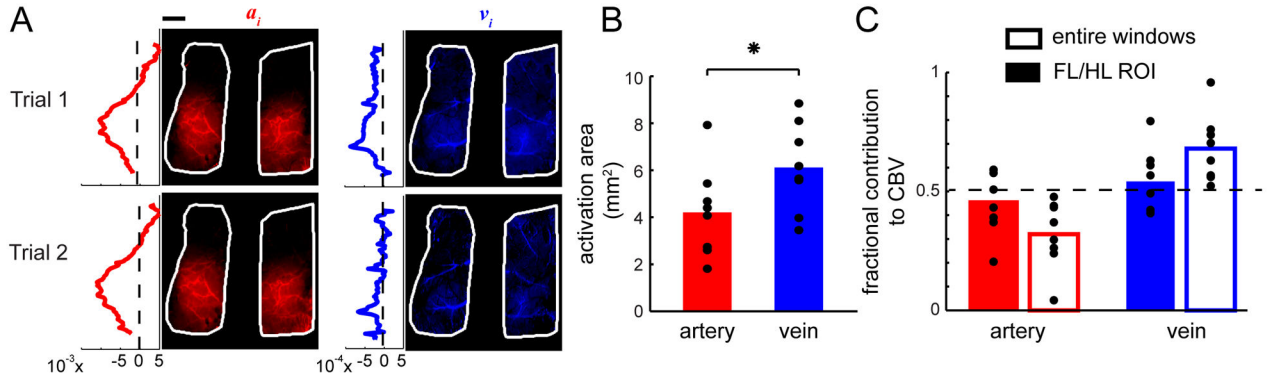


Figure 5. Spatially distinct arterial and venous contributions to cortical CBV changes during locomotion

(A) Fitted fast component, a_i (left), and slow component, v_i (right), of all pixels within ROI (white outline) for two different trials. The fast components reliably recovered the arterial network; while the slow components recovered the venous network. Side plots show the medial-lateral average of a_i (red) and v_i (blue) in the left hemisphere. Scale bar = 1 mm. (B) The mean area of arterial (red) or venous (blue) map of pixels with fit amplitudes greater than 50% of the peak response. The peak is defined as the 99%tile of the arterial or venous component amplitude response over the entire window. Activated areas of individual mice are shown in black dots. *: $p < 0.05$. (C) Average fractional contributions to the dynamic component of CBV response for arteries (red), or veins (blue), over the entire window (white bars), or only the SI FL/HL area (filled bars). $N = 8$ mice.

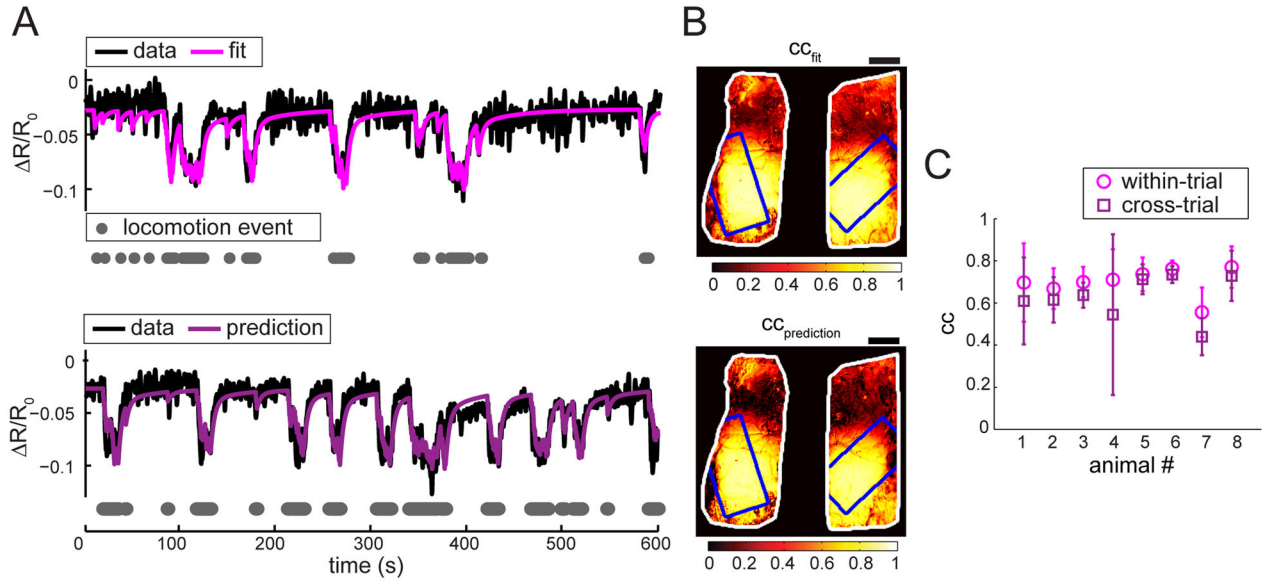


Figure 6. Fitted HRFs are stable across trials

(A) Example of cross-validation of fit parameters. Averaged IOS across all pixels within the SI FL/HL area (blue polygon in (B)), all model parameters were fitted to one trial ('fit', upper panel, $cc=0.83$) and applied to another trial ('prediction', lower panel, $cc=0.86$). (B) Goodness-of-fit, measured by correlation coefficients between measured data and model fit, of within-trial fitting, cc_{fit} (upper panel), and of cross-trial prediction, $cc_{prediction}$ (lower panel), in the entire window. Blue polygons enclose SI FL/HL area in each hemisphere. Scale bars = 1 mm. (C) Comparing the average cc within the SI FL/HL area, with error bars, of within-trial (magenta) and cross-trial (purple) estimates for each animal. $N=8$ mice.

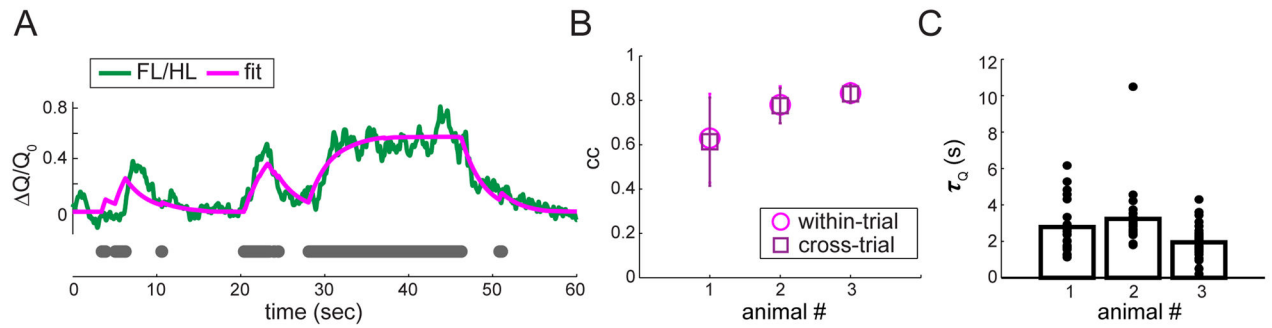


Figure 7. Locomotion-induced changes in CBF have linear dynamics

(A) Example of fitting the linear model (*magenta*) to 60-second trial of fractional change of CBF from baseline, \bar{Q}/\bar{Q}_0 (*green*), in the FL/HL representation. Locomotion events are shown as gray dots. (B) Comparison of average cc between within-trial model fitting (*magenta circle*) and cross-trial prediction (*purple square*), with error bars, for all 3 animals. (C) Fitted time constants, τ_Q , of all trials (*black dots*) averaged for each animal (*bars*).